Journal of Materials Chemistry A

Intrinsically Zwitter-ionic COF: Carboxylic Acid and Pseudo-tetrahedral sp^3 Nitrogen Functionalized Covalent Organic Framework with Potential for Humidity Sensing

Journal:	*Journal of Materials Chemistry A*
Manuscript ID	TA-ART-09-2023-005416.R1
Article Type:	Paper
Date Submitted by the Author:	24-Oct-2023
Complete List of Authors:	Nandi, Shyamapada; IISER Pune, Chemistry; Vellore Institute of Technology Singh, Himan; IISER Pune, Chemistry Shekhar, Pragalbh; IISER Pune, Chemistry Chakraborty, Debanjan; Indian Institute of Science Education Research Pune, CHEMISTRY; Kushwaha, Rinku; IISER Pune, Chemistry Ramanathan, Vaidhyanathan; IISER Pune, Chemistry

ARTICLE

Intrinsically Zwitter-ionic COF: Carboxylic Acid and Pseudo-tetrahedral *sp³* Nitrogen Functionalized Covalent Organic Framework with Potential for Humidity Sensing

Received 00th January 20xx,
Accepted 00th January 20xx

DOI: 10.1039/x0xx00000x

Shyamapada Nandi,*[a],¥ Himan Dev Singh,[b],¥ Pragalbh Shekhar,[b] Debanjan Chakraborty,[b] Rinku Kushwaha [b] and Ramanathan Vaidhyanathan*[b][c]

Herein, we report a zwitter-ionic Covalent Organic Framework (COF) simultaneously functionalized with carboxylic acid and protonatable sp^3 nitrogen. The acidity and basicity of these functional groups are so well balanced that they can be easily protonated and deprotonated by water/humidity. Color changes visibly display the dry and wet states. We believe that in the presence of moisture, it becomes zwitter-ionic, with the carboxylic acid getting deprotonated and concertedly protonating the sp^3 nitrogen centers. This directly impacts the extent of conjugation in the carboxylate group carrying module of the COF, triggering the color change. This was corroborated by a lack of color change under humidity when a structurally equivalent COF devoid of the carboxylic acid groups was employed. The pseudo-tetrahedral sp^3 nitrogen centers and the freely rotatable bulky carboxylic acid group in the framework's backbone weaken the π-stacking between the COF layers; this allows the COF to exfoliate into nanosheets with ease. The organic dispersions of these nanosheets are highly luminescent under UV radiation. A trace quantity of water in the organic solvent completely quenches the luminescence, enabling the COF to act as a moisture sensor for organic solvents with a very impressive detection limit (LOD = 0.027% in acetonitrile; LOD = 0.128% in acetone). A Gaussian calculation reveals an alteration in the frontier orbitals between the zwitterionic vs. acid forms. While DFT and MD modeling studies reveal that though the water's interaction with the COF is not strong, it is kinetically favored, which is key to reversible protonation-deprotonation chemistry. Thus, this designer COF represents an applicable solid-state humidity/water sensing material.

Introduction

Controlling humidity is an important target in several sectors, such as automobiles, indoor-air-management, battery-production, pharmaceutical and food industries, chemical and biological reactions.[1-6] For example, it is necessary to control the humidity (Relative Humidity of 40-60% according to the US Environmental Protection Agency) of the indoor environment where people spend a substantial amount of time daily.[7] Besides our daily life, humidity plays a major role in several chemical/biological processes.[8-11] In many cases, the reactions work only under inert and moisture-free conditions.[12,13] Also, the yields and the purity of the products formed can be very sensitive to the amount of moisture in the reaction/solvents. It plays a critical role in organometallic chemistry where traces of water in the solvent can lead to explosion and fire accidents.[14] The presence of moisture in petroleum-based fuels can compromise the performance and life of the engines due to clogged fuel channels at low temperatures. The use of humidity sensors in such cases becomes inevitable. In the automotive industry, these humidity sensors are used in rear window defoggers and motor assembly lines; in the pharmaceutical industry, they are used in respiratory equipments,[15] sterilizers, incubators,[16] pharmaceutical processing[2] and biological products;[16] and in the food processing industry,[2] they find application in dryers, ovens, film desiccation, paper and textile production.[17] That is why there is an ever-growing demand for humidity sensors in every sector, including our daily lives.

In this regard, porous crystalline materials can be very efficient in humidity sensing and humidity control depending on the pore size and different functionalities incorporated into the structure by design.[18-20] Covalent organic frameworks are a relatively new class of metal-free crystalline, ordered and porous polymers that have gained

[a]Dr. S. Nandi
Chemistry Division, School of Advanced Sciences, Vellore Institute of Technology, 600127, Chennai, India.
E-mail: shyamapada.nandi@vit.ac.in
[b]H. D. Singh, P. Shekhar, Dr. D. Chakraborty, R. Kushwaha, Dr. R. Vaidhyanathan
Department of Chemistry
Indian Institute of Science Education and Research, 411008, Pune, India
[c]Dr. R. Vaidhyanathan
Centre for Energy Sceince
Indian Institute of Science Education and Research, 411008, Pune, India
E-mail : vaidhya@iiserpune.ac.in
¥ These authors contributed equally
Electronic Supplementary Information (ESI) available: [details of any supplementary information available should be included here]. See DOI: 10.1039/x0xx00000x

significant interest in the past decade for various applications such as gas separation and storage,[21-24] biomedical applications,[25] charge storage,[26-29] heterogeneous catalysis,[30-36] photocatalysis,[37-39] optics,[40-42] sensing,[43-50] and bioimaging.[51] Recently, different functionalized COFs have found use in sensing such as pH sensing,[52,53] HCl/acidic vapor sensing,[44,45] water contaminant sensing,[47] etc. In addition to these applications, these novel materials have started to gain interest in humidity/water sensing applications.[19,54-56] For instance, Auras and coworkers have reported pyrene-based COF showing color shifts on water exposure and other volatile solvent vapors.[49] This COF shows a very good response time for humidity sensing, but the change in the absorption spectrum is very small (the shift is 20-30 nm) upon exposure to humidity. Marder and co-workers reported humidity sensing in covalent organic frameworks through a reversible isomerization in an imine-based COF.[54] This COF system also shows a rapid response with color change visible to the naked eye. Kaskel and co-workers have recently reported chemically stable carbazole-based COFs for humidity control applications.[18] However, these COFs are developed from ligands that need to be synthesized in multistep reactions, making these COFs quite expensive. The COFs made from relatively simple linkers would be a better candidate for sensing-type applications. Also, finding new chemical principles governing such humidity-triggered color changes adds immense value. In this work, we have developed a novel –COOH functionalized COF from simple and cheap linkers that show a dramatic color change (visible to the naked eye) on exposure to moisture. When dispersed in different organic solvents, this COF shows a photoluminescent character upon excitation with UV radiation. We have further utilized this COF's property for sensing water traces in various organic solvents such as acetone, acetonitrile (ACN) etc. The dramatic color change of the framework was attributed to its water-induced protonation/deprotonation. DFT/Gaussian-based molecular simulations further supported this.

Result and Discussion

Synthesis of IISERP-COF31 (1): The tripodal aldehyde, tris[4-formylphenyl] amine and dipodal amine (with an angle of 120° between the two -NH_2 groups) 3,5-diaminobenzoic acid were employed to synthesize the Schiff bonded COF bearing the *sp*^{3} nitrogen and free -COOH group in it. A typical synthesis was carried out solvothermally via the condensation of the aldehyde and the amine in a mixture of mesitylene, o-dichlorobenzene and ethanol at 120°C for 72 hours (Figure 1A and Scheme S1). The solvothermal

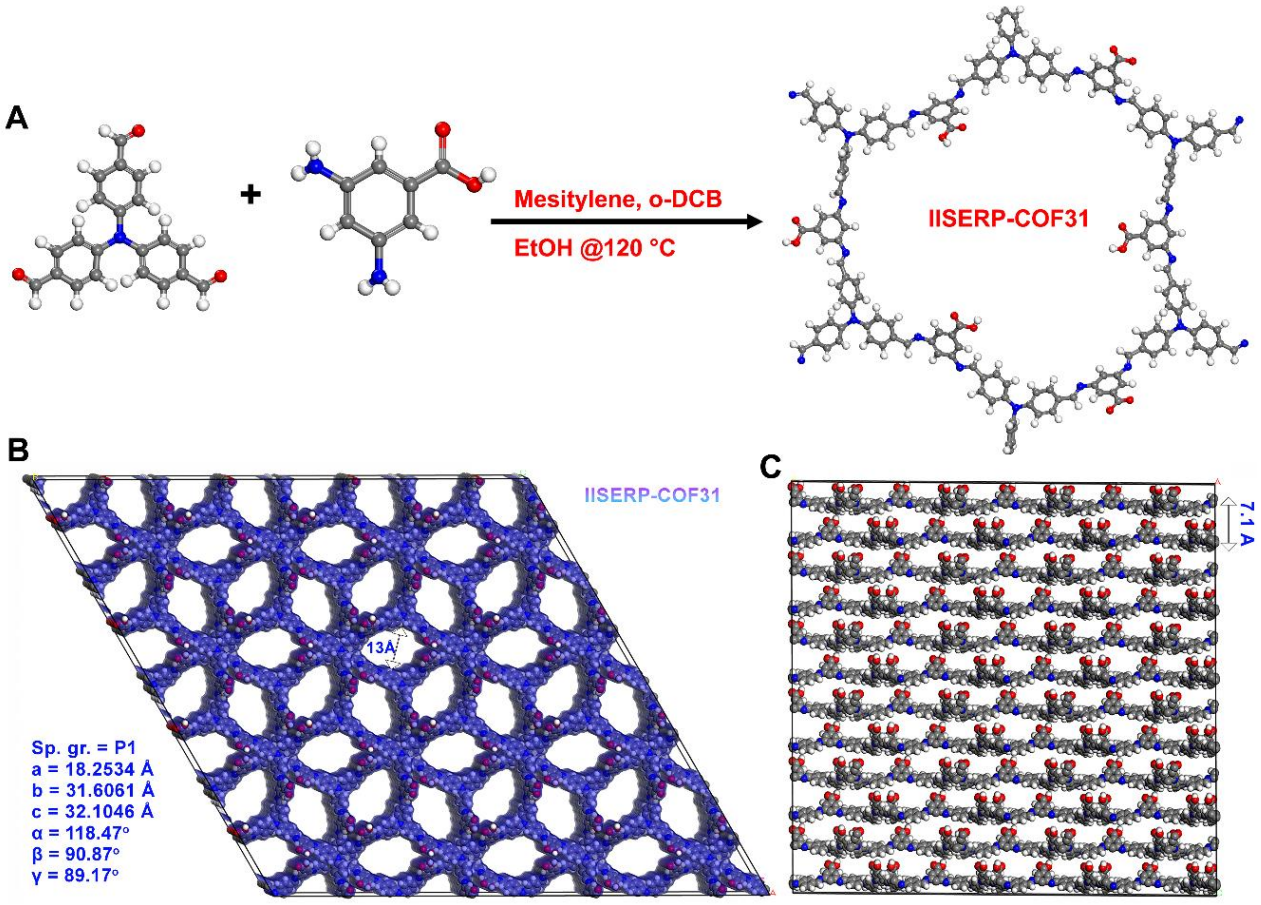

Figure 1. A: A schematic diagram of the COOH functionalized COF (**1**) with synthetic details. Note: The polymerized structure is just a chemdraw representation to indicate the framework connectivity and not the solved structure. **B:** Connolly representation (probe radius: 1.4Å) of the DFT-optimized structure of **1** showing the small pores. **C:** The layer stacking of **1**. The carboxylic acid moieties protrude into the interlayer spaces. Color code: C – grey, N – blue, O – Red, H – White.

reaction produces an orange-yellow powder, which was washed thoroughly with ethanol. This powder was further subjected to routine characterization such as powder XRD diffraction, thermogravimetric analysis (TGA), porosity analysis, FTIR and solid-state NMR spectroscopy. Strikingly, this COF turns to a bright red color on exposure to the atmosphere (humidity); the original orange color is regained if the sample is dried. To obtain a good PXRD pattern, we used the wet sample, which was directly collected from the synthesis tube with a small amount of the solvents to avoid exposure to atmospheric humidity.

Structure Solution:

A two-dimensional (2D) structure consisting of puckered hexagonal layers in agreement with the experimentally observed powder X-ray pattern of IISERP-COF31 (**1**) was modelled using the Material Studio program (Figure 1B, S1-S3). We followed a similar technique for the structure solution as presented in our earlier works.[35,57] Accordingly, the PXRD was indexed using the XCELL program to identify the suitable space group (P1 (FOM: >20). Following this, the model was constructed in a triclinic cell. The presence of asymmetrically placed carboxylic acid and sp^3 nitrogen moiety tends to such low symmetry. This structure was geometry optimized using tight-binding density functional theory (DFTB) algorithm embedded in the Materials Studio. In the optimized geometry, the structure adopts a P1 space group. A Pawley refinement of the powder pattern against the modeled cell was performed to generate the final structure (a = 18.2534 Å; b = 31.6061 Å; c = 32.1046 Å; α = 118.47 °, β = 90.87 °, γ = 89.17 °; Rp = 4.20 and wRp = 5.58). Unlike normal hexagonal 2D COFs, the layers of this COF are buckled because of the presence of sp^3 nitrogen centers in the aldehyde core.[58] The framework could be solved equally well for the eclipsed as well as the staggered geometry (Figure 2, S2, S4). Hence, we rationalized the potential structure of the COF via experimental porosity (Figures 2C and 2D). Note: The porosity for every phase was established using multiple batches of samples and from different instruments (Micromeritics ASAP 2020 and 3-flex). The structure wherein the layers are organized with an eclipsed configuration would have had a large pore size of 29.1 x 26.7 Å (Figure S1), which is not the case. The staggered lattice with a pore size of 13.0 Å (Figure 1B) gives a good Pawley fit and agrees well with the experimentally determined pore sizes. Due to the propeller-like configuration around the sp^3 nitrogen, the flat layers are not favored; instead, distinctly buckled layers are formed, and they are slipped over each other to give an *ABAB…* type stacking (Figure 1C). This gives the framework a pseudo-3D structure, and the layers are held together rather weak van der Waals and hydrogen-bond type interactions, unlike the archetypal flat layers found in COFs constructed from pi-stacking planar building units.

Bulk Characterization:

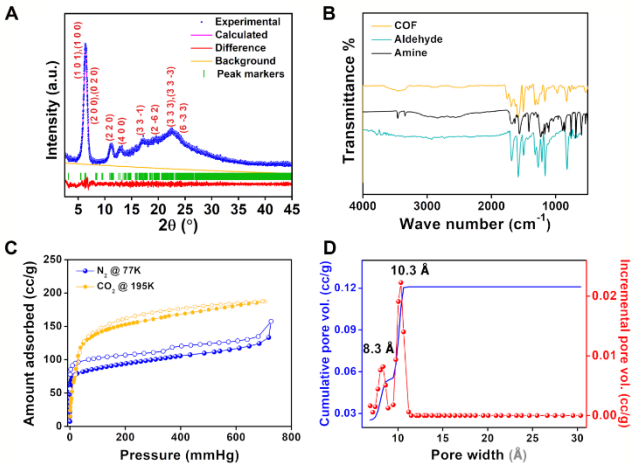

Figure 2. (A) The fit obtained from Pawley refinement of **1**. Final refinement parameters, Rp = 4.20 and wRp = 5.58. (B) FTIR spectra of **1** compared with that of the starting monomers, aldehyde and the amine. The spectrum of **1** shows the presence of free -COOH groups. (C) N_2 (77K) and CO_2 (195K) isotherms of **1** showing the microporous nature of the COF. (D) Pore size distribution plot of **1** calculated from the 77K N_2 isotherm using the NLDFT model.

The solid product of the solvothermal reaction was first characterized by Powder X-ray diffraction (PXRD). The as-made wet sample shows an intense low angle peak (2θ = 6.25°) and several other peaks, which are indexed based on the crystalline model, confirming the successful synthesis of a crystalline material (Figure 2A).

However, exposing **1** to the atmosphere followed by heating it in the oven at 90°C shows a rise in the intensity of peaks at 2θ = 18° and 23° corresponding to the interlayer spacing related reflections, which hints towards the possible disruption of the layer stacking (Figure S5). As the structure modeling suggests, weakly π-stacked layers are present in the framework, which a gentle external stimulus can easily exfoliate. The COF powder was exposed to air and heated at higher temperatures under a vacuum to achieve added exfoliation. The post-heated samples showed a further increase in the intensity of the interlayer spacing related reflections expected with the exfoliation of COF (Figure S5). Hence, it was realized that exfoliated material is a more thermodynamically favorable phase than the as-made COF. Therefore, all the measurements and experiments (unless mentioned) in this study were conducted on the exfoliated Covalent Organic Nanosheets (CONs).

Thermogravimetry analysis of **1** shows that the framework maintains its integrity up to a temperature of 350°C (Figure S6), which confirms that the intensity changes in the PXRD of samples heated at lower temperatures are not due to the breakdown of the covalent bonds present in the COF layers. Fourier transform infrared (FTIR) spectra of the **1** suggest the absence of the peaks corresponding to the diamine group, which indicates the full consumption of NH_2 groups of monomers. The typical vibration band due to C=N at 1586 cm^{-1} was observed along with the other bands (C=O, 1753 cm^{-1}) and (O-H, 3448 cm^{-1}) corresponding to the framework. The bands corresponding to C=O and O-H confirm the integrity of the -COOH group in the framework unambiguously (Figure 2B). The formation of Schiff bonds was further confirmed by solid-state ^{13}C magic angle spinning NMR spectra, which show a peak at δ = 155 ppm. Also, the peak corresponding to the carboxylic group could be observed from the ^{13}C NMR spectrum (Figure S7). The permanent porosity of **1** has been established by N_2 and CO_2 adsorption at 77K and 195K, respectively. The N_2 adsorption at 77K shows Type I isotherm, a characteristic of microporous material, with a saturation uptake of 120 cc/g (Figure 2C). A non-local density functional theory (NLDFT) fit to the adsorption branch of nitrogen isotherm yields a major pore size of 10.3 Å and 8.3 Å, which matches the structure (Figure 2D). The Brunauer–Emmet–Teller (BET) and Langmuir surface areas were estimated to be 340 and 520 m^2/g, respectively (Figure S8). Similarly, CO_2 shows a type I isotherm (at 195K) with higher uptake than N_2 (Figure 2). The morphological studies of **1** were conducted using Field Emission Scanning Electron Microscopy (FE-SEM). **1** has a cotton-ball-like morphology with small spikes (Figure 3A, S9, S10). These spikes are the small nano-crystallites of **1**, and these crystallites have aggregated to form the cotton ball-like structure. Furthermore, it could be observed from the High-Resolution Transmission Electron Microscopy (HRTEM) images that these cotton balls are made up of aggregated flakes (Figure 3B and S11). It is noteworthy to mention that we could observe the lattice fringes in the HRTEM images (Figure S11) indicating the high degree of crystallinity of the material.

As mentioned, **1** can easily exfoliate via exposure to the atmosphere, followed by thermal treatment. Due to this exfoliation, the number of π-stacked layers decreases and results in the formation of nanosheets, which contain very few π-stacked layers. In this case, atomic force microscopy (AFM) was used to probe the thickness of the nanosheets. The images taken from AFM showed the formation of covalent organic nanosheets (CONs) with an average thickness of ~4-6 nm (Figure 3C, 3D and S12). The Tyndall effect also confirmed the formation of nanosheets. **1** was soaked in different solvents in glass vials and sonicated for 10 minutes; after this, laser light was shed onto these vials from one end after regular intervals. The path of light through the solution could be traced even when it is kept undisturbed for 6 hours, which implies that the dispersed material didn't settle down on long-standing. It again proves the colloidal stability of nanosheets in the solutions (Figure 3, S13). The average size of the nanosheets was found to be between 500-600 nm, as confirmed by the dynamic light scattering (DLS) experiments performed on the exfoliated COF across three different batches (Figure S14). The easy exfoliation of **1** is in good agreement with our previous observation, where an imine bonded COF constructed from a 3,5-diamino-1,2,4-triazole (the angle between the two NH_2 group is closed to 120°) was found to be self-exfoliated during the synthesis itself.[59]

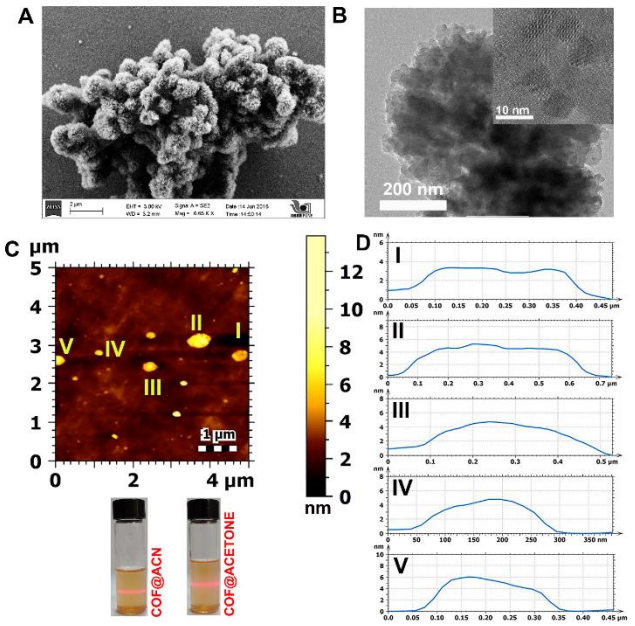

Figure 3. (A) FESEM image of **1** showing the cotton-ball like morphology with small spikes on it. (B) HRTEM image of **1** showing the flakes kind of structure. Inset showing the lattice fringes having inter planar distance of 0.26 nm which is very close to the interlayer distance obtained from the structural model. (C) (Top) AFM image of **1** showing the nanosheet character of it. (Bottom) **1** dispersed in different solvents showing the Tyndall effect for a prolonged time. (D) The height profile plot quantifies the thickness of the nanosheets to be in the range of ≈4-6 nm (see the Supporting Information for more images).

Optical studies:

Impressed by the drastic color change of **1** from yellow to bright red upon exposure to air, we recorded solid-state UV-vis spectra for both the samples, dry (yellow) and humidified (red) (Figure 4A). The dry one gives absorption maxima at 447 nm, whereas the humidity-exposed sample shows absorption maxima at 362 nm (Figure 4B). Direct optical band gap was calculated from the Tauc plot, and it was found that the band gap increases from 2.27 eV to 2.87 eV when the color of the sample changes from yellow to bright red (Figure 4C). We stored the sample under vacuum to trace the stimuli for the color change. The dry nitrogen and oxygen were passed over the sample (since N_2 and O_2 are major gases in the atmosphere) in two different experiments, but no change in the color of **1** was observed. Then, in a separate investigation, humid nitrogen and humid O_2 were passed over the sample in a similar fashion, resulting in the sample's immediate color change from orange-yellow to red in both experiments. Hence, this set of four experiments concluded that the humidity is responsible for the color change, which is independent of the nature of the carrier gas.

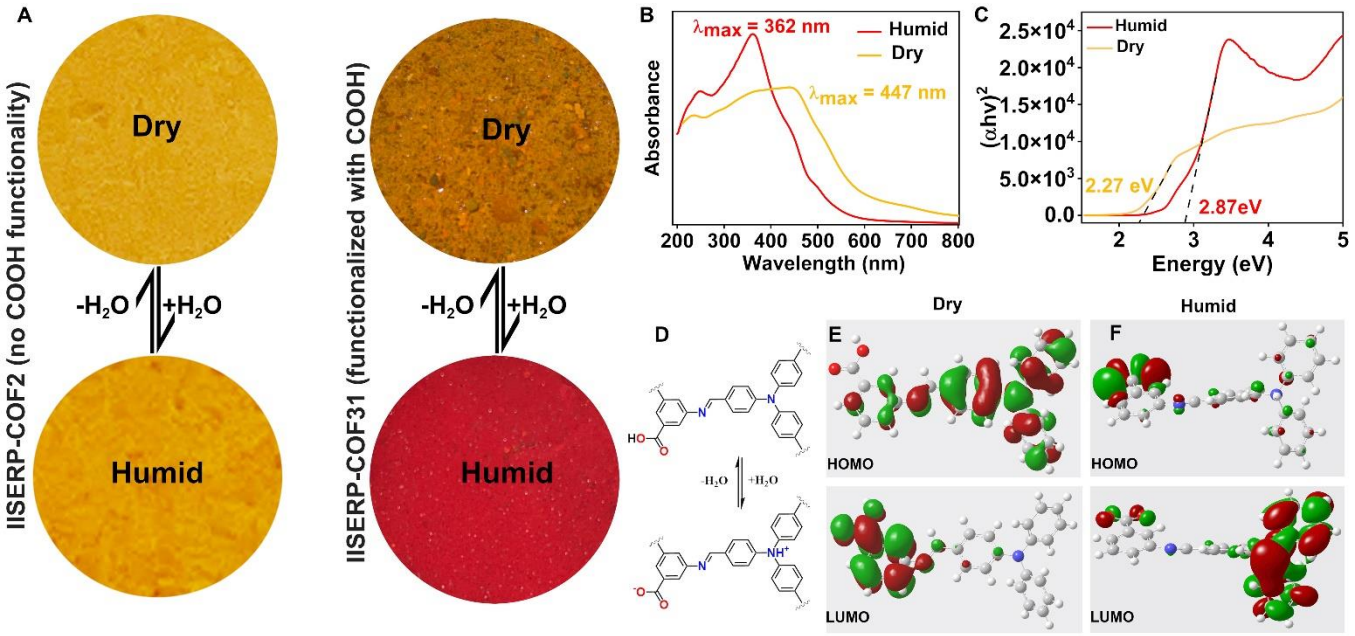

Figure 4. (A) A comparative photographic image of **1** and IISRRP-COF2 in dry and humid condition showing the visible colour change only in case of **1.** (B) Solid state UV-vis spectra of **1** in dry and humid condition showing the change in λ_{max} of the absorption spectra. (C) Tauc plot showing the direct bandgap derived from the UV-vis spectra. Note: the change in bandgap upon humidity exposure is in good agreement with the visible color change of **1**. (D) Schematic diagram showing the possible mechanism for the visible color change of **1**. (E) The frontier orbitals of the model compound in dry state derived from a DFT/Gaussian calculation. (F) The frontier orbitals of the model compound in humid condition derived from a DFT/Gaussian calculation.

The mechanism of the visible color change of the nanosheets was attributed to the water-induced protonation and deprotonation of the framework. For the dry sample, when there is no moisture in the system, the -COOH group of the framework is in neutral form (Figure S15). As soon as the moisture is introduced in the system, the framework converts to the zwitterionic form, where the sp^3 nitrogen of the aldehyde is protonated and the -COOH group is deprotonated (Figure 4D and S16). This COO^- thus generated by the humidity or water can supply more electrons into the conjugated system. This phenomenon is accountable for altering the frontier orbitals (HOMO and LUMO) of **1**, thereby responsible for the color change. Therefore, the simultaneous presence of the sp^3 nitrogen and the free terminal COOH group in the framework is necessary to observe such humidity-dependent color change. This was further proved by synthesizing a COF (IISERP-COF2)[58] where the sp^3 nitrogen is present but the -COOH group is absent. As expected, this COF shows no humidity-dependent color change (Figure 4A and S17). The role of water/protonated water is crucial to impart this effect. The XPS spectra of **1** (after exposure to atmospheric humidity) further support this protonation. As presented in Figure S18, the N1s spectrum shows a quaternary nitrogen site in **1**, indicating the protonation of the sp^3 nitrogen present in the framework. However, in the XPS spectra of IISERP-COF2 we did not observe any quaternary nitrogen.[58]

To shed more light on the mechanism of the visible color change, we resorted to DFT/Gaussian-based simulations. For this, we have created the smallest possible model compounds for the dry and humid conditions, as presented in Figure 4D. These model compounds were first geometry optimized using a DFT method embedded in Materials Studio. The optimized model compounds were then used for the Gaussian calculation using Density functional theory based on the B3LYP hybrid functional method with the 6-311G basis set.[60, 61] The extracted frontiers orbitals clearly show that in case of dry condition, the HOMO is located around the triphenylamine core of the aldehyde unit and the LUMO is located around the free -COOH group and the phenyl ring of the amine (Figure 4E). However, in the humid condition when **1** exists in the zwitterionic form, the HOMO is located around the -COO- group and the LUMO is located around the triphenylamine core of the aldehyde part (Figure 4F). This switching of the HOMO and LUMO between the dry and the humid model is responsible for the dramatic visual color change.

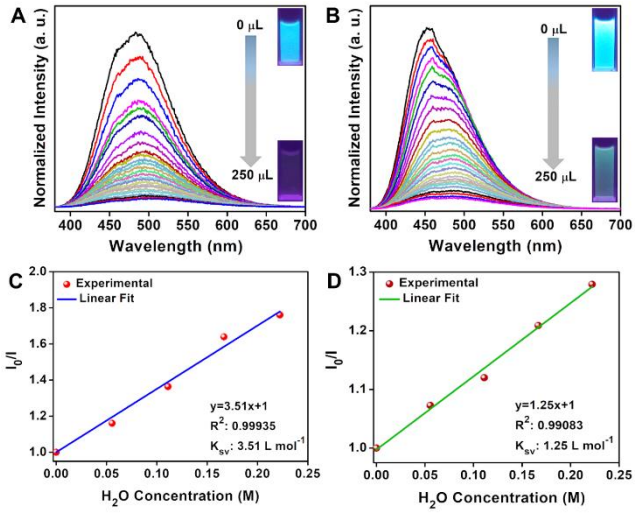

Figure 5. (A) PL Spectra of **1** dispersed in ACN showing the quenching of photo luminescence upon gradual addition of water (B) PL Spectra of **1** dispersed in acetone showing the quenching of photo luminescence upon gradual addition of water (C) A Stern- Volmer plot in the low water concentration in ACN showing the linearity. (D) A Stern-Volmer plot in the low water concentration in acetone showing the linearity.

Another important feature of **1** is its photoluminescent character. **1** dispersed in different organic solvents emits blue light upon excitation with UV radiation. However, the presence of water in the organic solvents quenches the luminescence. We have utilized this property of **1** for sensing trace amounts of water in different organic solvents. We first recorded the photoluminescence (PL) spectra of **1** in different solvents such as acetone, tetrahydrofuran (THF), dimethyl formamide (DMF), dimethyl acetamide (DMA), methanol (MeOH), ethanol (EtOH), dimethyl carbonate (DMC), Acetonitrile (ACN) etc at 30°C (Figure S19). The emission occurs at ~ 455-480 nm for all the verified solvents. However, the PL intensity was different for each solvent. To study the sensing of trace water in organic solvents, we chose two solvents, ACN and acetone. A small amount of **1** (5 mg) was dispersed in 2 ml of respective solvents, and PL spectra were recorded. Then, deionized water (2 µL to 250 µl) was added sequentially to the cuvette, and PL spectra were recorded after every addition of water. It was observed that even with the addition of a very small amount of water (2 µL), a remarkable change in the intensity of the peak in the PL emission spectra was observed. This quenching of the emission increases with further addition of water (Figure 5A and 5B). This decay in the emission with the addition of miniscule amounts of water shows the sensitivity of **1** towards moisture. In both the solvents, the fluorescence intensity decays very fast initially and then tends to slow down (Figure S20 and S21). Nearly 80% of the fluorescence intensity quenches by adding 1 vol% of water. The detection limit was calculated from a linear fit to the fluorescence intensity vs. water concentration (in the low-concentration region) graph. The limit of detection (LOD) was 0.027% and 0.128% in the case of ACN and acetone, respectively (Figure S20 and S21). It is noteworthy to mention that the LOD values are better or comparable to some of the best-known COFs/MOFs/Carbon materials for water sensing (Table S1). Notably, the sensing works the best in acetonitrile (ACN), in which the emission peak shows a sharp decrease in intensity with the addition of just 2 µL of water. This PL intensity goes to zero when the water content is increased to 250 µL. However, in the case of acetone, a decrease in the PL intensity of the emission peak is observed with successive addition of water, but

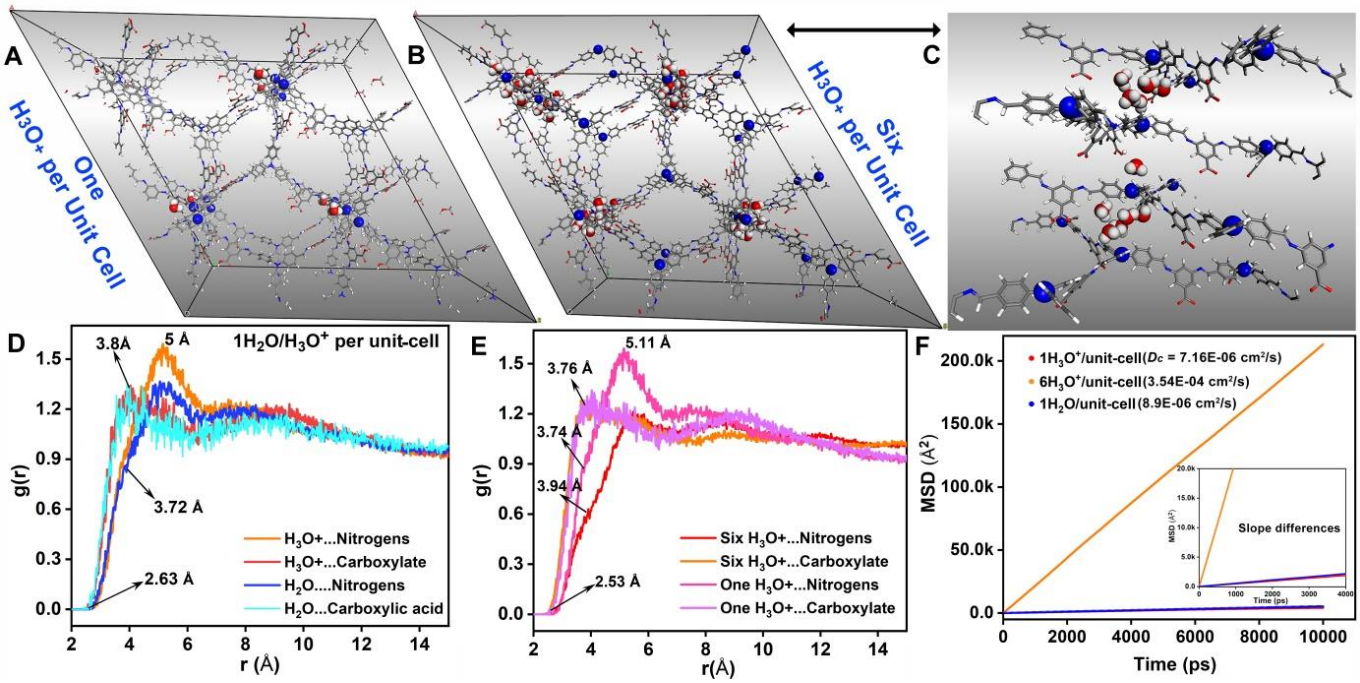

Figure 6. (A) A DFT-optimized structure of H_3O^+ in COF with a loading of $1H_3O^+$/unit-cell. The *sp*³ nitrogen and the protonated water sandwiched between them are shown in balls. (B) and (C) DFT-optimized structure of 6H3O+/unit-cell in **1** showing the protonated water sandwiched by the *sp*³ nitrogen from two different-layers. (D) and (E) The RDF plots from MD simulations of **1** with $1H_3O^+$ and $6H_3O^+$/unit-cell displaying the distances between the protonatable sites (donor) and the water molecules (acceptor). (F) The Mean square displacement vs. time plot from MD simulations showing the favourable diffusion for both neutral and protonated water inside the COF and with high H_3O^+ concentration, the diffusion coefficient rises drastically.

it doesn't decay to zero with the same amount of water. The same observation can be visualized in the optical images, which show complete switch ON and OFF sensing in the case of acetonitrile; however, in the case of acetone, the effect is not so prominent (Figure 5). This could be due to the higher polarity ACN (ε = 37.5) compared to acetone (ε = 20.7). Further, a Stern-Volmer plot in the low water content region shows linear behavior in both cases (Figure 5C and 5D), indicating a strong water interaction with **1** dispersed in ACN or acetone.[62] The Stern-Volmer coefficient was calculated to be 3.51 L mol^{-1} and 1.25 L mol^{-1} for the case of ACN and acetone, respectively. The sensing of the trace amount of water in organic solvents using **1** is highly reproducible (Figure S22-S23). It is important to mention that the material can be recovered after the 1st cycle by drying under vacuum, and the dried material can be used in the next cycle (Figure S24). The recyclability of the material was attributed to its good water stability, which was confirmed by the PXRD and FTIR study of the water-soaked sample (Figure S25). The humidity sensing by **1** was established in the solid state as well. The color of the as-made COF (orange-yellow) changes to bright red upon adding a drop of water to it (Figure S26). Also, this change is reversible, i.e., the color changes to yellow upon drying the COF in a vacuum. This color change is fully reversible and can be achieved for multiple cycles. Though these studies indicate that the water in the vapor form strongly interacts with the COF, the water adsorption isotherm suggests the opposite (Figure S27). We set out to address this incongruity.

Interaction of water and protonated water with the COF:

Considering the COF's immediate color response to even vapor phase water (humidity), one would expect an abrupt water uptake at low partial pressures in an isotherm. Against this expectation, the water isotherm was shallow with a nominal saturation capacity. To further verify this, we calculated the isosteric heat for a single water molecule as well as a protonated water molecule inside the COF in Henry's regime. It was very low (< 10 kcal/mol), which agrees well with the shallow low-pressure uptake observed from experimental isotherms. This suggests that sensing is not due to physisorptive uptake of water by the material. If we consider the alternative, a proton abstraction from COF's functional groups by water, it would be expected to be a lot more sensitive and efficient even at low water concentrations, which seems to be the case. Now, we realize that this water could be playing a key role in transferring the acidic proton present on the free carboxylic acid in the framework to these lone-pair containing sp^3 nitrogen centers, giving rise to the zwitter-ionic form with a markedly different color. To verify this, we attempted to identify the most-favorable position for the H_3O^+ in the COF, which again turned out to be the same space occupied by the neutral water (Note: one of the carboxylic acid groups was rendered as carboxylate during the introduction of the H_3O^+) (Figure 6).

The color change on the COF flake is quite rapid with the introduction of humidity (low water concentration); this is likely to be a diffusion-controlled kinetic process. Hence, we wanted to know how favorable it is for protonated water molecules to diffuse into the pores. This is extremely difficult to determine experimentally; therefore, we resorted to molecular dynamics. The optimized structure was equilibrated using an NPT ensemble, and the average lattice parameters were employed for the output structure. The migration of the protonated water/neutral water in the cationic framework was explored under the NVT conditions. The final trajectory was obtained from a 50 ns microcanonical NVE dynamics performed at 300 K. The Mean Square Displacement (MSD) vs. time plots were used to calculate the average diffusion coefficient for the guest species (Figure 6F). Importantly, the diffusion coefficient for the single protonated water per unit cell is 7.16E-06 cm^2/s; while that of neutral water is 8.9E-06 cm^2/s and for six protonated water per unit cell, it is 3.54E-04 cm^2/s. These are extremely favorable, and such high values support the rapid sensing of humidity by the COF material. The build-up of more and more protonated water improves their self-diffusion, most likely through cooperativity. Also, these high diffusion values suggest that this humidity sensing is not a mere surface phenomenon but a diffusion-controlled process. Importantly, a broader insight develops: for these solid-state sensing, one need not have strong equilibrium interactions between the guest and the host; rapid diffusion-controlled kinetics is the key.

Conclusion:

In conclusion, we have developed for the first-time a -COOH functionalized and sp^3 N rich imine bonded COF which can be easily exfoliated to nanosheets of few nm thicknesses. This COF reversibly changes its color from orange-yellow to bright red when exposed to humidity. This dramatic color change could be used for developing potential humidity sensors. We attributed this color change to the humidity dependent protonation or deprotonation of the tertiary amine and free -COOH group present in the framework. This was further supported by the DFT/Gaussian based calculation. Furthermore, the nanosheets dispersed in organic solvents emits blue light upon excitation with UV radiation. This luminescence completely quenches upon addition of small quantity of water. This property of the COF has been utilized for detection of trace quantity of water in different organic solvents. This study would help designing future generation COF based humidity sensor.

Experimental

Synthesis of IISERP-COF31:

Tris[4-formylphenyl]amine (0.25 mmol) and 3,5-diaminobenzoic acid (0.37 mmol) were added in a pyrex tube and dissolved in 2ml mesitylene, 3 ml o-dichlorobenzene and 4 ml ethanol. 0.25 ml acetic acid was added to this mixture and was stirred well. The pyrex tube was then flash frozen using liquid nitrogen and sealed. The contents in the sealed tube were heated at 120°C for 3 days. After cooling to room temperature, the light-yellow precipitate was filtered and washed with DMF, THF, MeOH. Isolated yield was 76% with respect to the aldehyde. The

solid was characterized using FTIR & ^{13}C-NMR Spectra, FESEM & TEM microscopy etc.

Conflicts of interest

"There are no conflicts to declare".

Acknowledgements

SN thanks Vellore Institute of Technology, Chennai and IISER, Pune. HDS and PS thank CSIR for fellowship. VR acknowledge IISER-Pune for the necessary funding. DC thanks DST-Inspire for financial assistance. RK thanks AFOSR under award number FA2386-21-1-4022 for financial support. We acknowledge the SERB (CRG/2021/008250), MHRD-FAST (MHRD Project 150 (F.No.5-5/2014-TS-VII & F.No. 22-2/2016-TS-II/TC)). We gratefully acknowledge the DST Material for Energy Storage program (DST/TMD/MES/2k17/103), Air Force Office of Scientific Research (AFOSR) under award number FA2386-21-1-4022, MHRD-STARS program (STARS/APR2019/CS/278/FS) and the "DST-Nanomission under the Thematic Unit Program" (EMR/2016/003553) for the financial support. We acknowledge National Supercomputing Mission (NSM) for providing computing resources of 'PARAM Brahma' at IISER Pune, which is implemented by C-DAC and supported by the Ministry of Electronics and Information Technology (MeitY) and Department of Science and Technology (DST), Government of India.

Notes and references

1 A. Baughman and E. A. Arens, *ASHRAE trans.*, 1996, **102**, 192-211.
2 D. Bridgeman, J. Corral, A. Quach, X. Xian and E. Forzani, *Langmuir*, 2014, **30**, 10785-10791.
3 K. Nagaya, T. Senbongi, Y. Li, J. Zheng and I. Murakami, *Appl. Therm. Eng.*, 2006, **26**, 1545-1551.
4 A. Marchetti, S. Pilehvar, L. Hart, D. L. Pernia, O. Voet, W. Anaf, G. Nuyts, E. Otten, S. Demeyer, O. Schalm, K. D. Wael, *Build Environ*., 2017, **126**, 132-146.
5 A. TenWolde, C. L. Pilon, Proceedings of thermal performance of the exterior envelopes of whole buildings X, 2007.
6 H. Goderis, G. Ampe, M. Feyten, B. Fouwe, W. Guffens, S. Van Cauwenbergh and P. Tobback, *Biotechnol. Bioeng.*, 1987, **30**, 258-266.
7 W. H. Organization, Air quality guidelines: global update 2005: particulate matter, ozone, nitrogen dioxide, and sulfur dioxide, 2006.
8 F. Puppo, A. Dave, M.-A. Doucey, D. Sacchetto, C. Baj-Rossi, Y. Leblebici, G. De Micheli and S. Carrara, *IEEE Trans. Nanobiosci.,* 2014, **13**, 19-30.
9 D. Dobrynin, G. Friedman, A. Fridman and A. Starikovskiy, *New J. Phys.*, 2011, **13**, 103033.
10 R. Reich and L. Morien, *Appl.Environ.Microbiol.*, 1982, **43**, 609-614.
11 L. Monico, A. Chieli, S. De Meyer, M. Cotte, W. de Nolf, G. Falkenberg, K. Janssens, A. Romani and C. Miliani, *Chem.Eur.J*, 2018, **24**, 11584-11593.
12 K. L. Vikse, M. P. Woods and J. S. McIndoe, *Organometallics*, 2010, **29**, 6615-6618.
13 J. A. Mosely, P. Stokes, D. Parker, P. W. Dyer and A. M. Messinis, *Eur. J. Mass Spectrom.*, 2018, **24**, 74-80.
14 H. W. Roesky, M. G. Walawalkar and R. Murugavel, *Acc. Chem. Res.*, 2001, **34**, 201-211.
15 J. Dai, H. Zhao, X. Lin, S. Liu, Y. Liu, X. Liu, T. Fei and T. Zhang, *ACS Appl. Mater. Interfaces*, 2019, **11**, 6483-6490.
16 G. Korotcenkov, Handbook of humidity measurement, volume 2: Electronic and electrical humidity sensors, CRC Press, 2019.
17 S. Rauf, M. T. Vijjapu, M. A. Andrés, I. Gascón, O. Roubeau, M. Eddaoudi and K. N. Salama, *ACS Appl. Mater. Interfaces*, 2020, **12**, 29999-30006.
18 L. Gilmanova, V. Bon, L. Shupletsov, D. Pohl, M. Rauche, E. Brunner and S. Kaskel, *J. Am. Chem. Soc.*, 2021, **143**, 18368-18373.
19 S. Jhulki, A. M. Evans, X.-L. Hao, M. W. Cooper, C. H. Feriante, J. Leisen, H. Li, D. Lam, M. C. Hersam, S. Barlow, J.-L. Brédas, W. R. Dichtel and S. R. Marder, *J. Am. Chem. Soc.*, 2020, **142**, 783-791.
20 F. Haase and B. V. Lotsch, *Chem. Soc. Rev.*, 2020, **49**, 8469-8500.
21 M. S. Lohse and T. Bein, *Adv. Funct. Mater.*, 2018, **28**, 1705553.
22 H. Wei, S. Chai, N. Hu, Z. Yang, L. Wei and L. Wang, *Chem. Commun.*, 2015, **51**, 12178-12181.
23 Y. Zeng, R. Zou and Y. Zhao, *Adv.Mater.*, 2016, **28**, 2855-2873.
24 N. Huang, R. Krishna and D. Jiang, *J. Am. Chem. Soc.*, 2015, **137**, 7079-7082.
25 A. Esrafili, A. Wagner, S. Inamdar and A. P. Acharya, *Adv. Healthcare Mater.,* 2021, **10**, 2002090.
26 C. R. Mulzer, L. Shen, R. P. Bisbey, J. R. McKone, N. Zhang, H. c. D. Abruña and W. R. Dichtel, *ACS Cent. Sci.*, 2016, **2**, 667-673.
27 R. Kushwaha, S. Haldar, P. Shekhar, A. Krishnan, J. Saha, P. Hui, C. P. Vinod, C. Subramaniam and R. Vaidhyanathan, *Adv. Energy Mater.*, 2021, **11**, 2003626.
28 S. Kandambeth, V. S. Kale, O. Shekhah, H. N. Alshareef and M. Eddaoudi, *Adv. Energy Mater.*, 2022, **12**, 2100177.
29 Z. Tian, V. S. Kale, Y. Wang, S. Kandambeth, J. Czaban-Jozwiak, O. Shekhah, M. Eddaoudi and H. N. Alshareef, *J. Am. Chem. Soc.*, 2021, **143**, 19178-19186.
30 Y. Li, W. Chen, R. Gao, Z. Zhao, T. Zhang, G. Xing and L. Chen, *Chem. Commun.*, 2019, **55**, 14538-14541.
31 Y. Zhi, Z. Wang, H. L. Zhang and Q. Zhang, *Small*, 2020, **16**, 2001070.
32 J. Guo and D. Jiang, *ACS Cent. Sci.*, 2020, **6**, 869-879.
33 D. Mullangi, D. Chakraborty, A. Pradeep, V. Koshti, C. P. Vinod, S. Panja, S. Nair and R. Vaidhyanathan, *Small*, 2018, **14**, 1801233.
34 D. Chakraborty, P. Shekhar, H. D. Singh, R. Kushwaha, C. Vinod and R. Vaidhyanathan, *Chem Asian J.*, 2019, **14**, 4767-4773.
35 D. Chakraborty, S. Nandi, D. Mullangi, S. Haldar, C. P. Vinod and R. Vaidhyanathan, *ACS Appl. Mater. Interfaces*, 2019, **11**, 15670-15679.
36 C. Chandran, H. D. Singh, L. S. Leo, P. Shekhar, D. Rase, D. Chakraborty, C. P. Vinod and R. Vaidhyanathan, *J. Mater. Chem. A,* 2022, **10**, 15647-15656.
37 L. Stegbauer, K. Schwinghammer and B. V. Lotsch, *Chem. Sci.*, 2014, **5**, 2789-2793.
38 K. Gottschling, G. k. Savasci, H. Vignolo-González, S. Schmidt, P. Mauker, T. Banerjee, P. Rovó, C. Ochsenfeld and B. V. Lotsch, *J. Am. Chem. Soc.*, 2020, **142**, 12146-12156.

39 S. Wan, J. Guo, J. Kim, H. Ihee and D. Jiang, *Angew.Chem.Int.Ed.*, 2009, **48**, 5439-5442.
40 E. Jin, J. Li, K. Geng, Q. Jiang, H. Xu, Q. Xu and D. Jiang, *Nat. Commun.*, 2018, **9**, 1-10.
41 S. Haldar, D. Chakraborty, B. Roy, G. Banappanavar, K. Rinku, D. Mullangi, P. Hazra, D. Kabra and R. Vaidhyanathan, *J. Am. Chem. Soc.*, 2018, **140**, 13367-13374.
42 P. Das, G. Chakraborty, S. Tyagi and S. K. Mandal, *ACS Appl. Mater. Interfaces*, 2020, **12**, 52527-52537.
43 X. Liu, D. Huang, C. Lai, G. Zeng, L. Qin, H. Wang, H. Yi, B. Li, S. Liu and M. Zhang, *Chem. Soc. Rev.*, 2019, **48**, 5266-5302.
44 A. F. EL‐Mahdy, A. M. Elewa, S. W. Huang, H. H. Chou and S. W. Kuo, *Adv. Optical Mater.*, 2020, **8**, 2000641.
45 L. Ascherl, E. W. Evans, J. Gorman, S. Orsborne, D. Bessinger, T. Bein, R. H. Friend and F. Auras, *J. Am. Chem. Soc.*, 2019, **141**, 15693-15699.
46 G. Das, B. P. Biswal, S. Kandambeth, V. Venkatesh, G. Kaur, M. Addicoat, T. Heine, S. Verma and R. Banerjee, *Chem. Sci.*, 2015, **6**, 3931-3939.
47 P. Albacete, A. López-Moreno, S. Mena-Hernando, A. E. Platero-Prats, E. M. Pérez and F. Zamora, *Chem. Commun.*, 2019, **55**, 1382-1385.
48 H.-L. Qian, C. Dai, C.-X. Yang and X.-P. Yan, *ACS Appl. Mater. Interfaces*, 2017, **9**, 24999-25005.
49 L. Ascherl, E. W. Evans, M. Hennemann, D. Di Nuzzo, A. G. Hufnagel, M. Beetz, R. H. Friend, T. Clark, T. Bein and F. Auras, *Nat. Commun.*, 2018, **9**, 1-8.
50 A. F. El-Mahdy, M.-Y. Lai and S.-W. Kuo, *J. Mater. Chem. C*, 2020, **8**, 9520-9528.
51 P. Wang, F. Zhou, C. Zhang, S.-Y. Yin, L. Teng, L. Chen, X.-X. Hu, H.-W. Liu, X. Yin and X.-B. Zhang, *Chem. Sci.*, 2018, **9**, 8402-8408.
52 L. Chen, L. He, F. Ma, W. Liu, Y. Wang, M. A. Silver, L. Chen, L. Zhu, D. Gui and J. Diwu, *ACS Appl. Mater. Interfaces*, 2018, **10**, 15364-15368.
53 Y. Zhang, X. Shen, X. Feng, H. Xia, Y. Mu and X. Liu, *Chem. Commun.*, 2016, **52**, 11088-11091.
54 S. Jhulki, A. M. Evans, X.-L. Hao, M. W. Cooper, C. H. Feriante, J. Leisen, H. Li, D. Lam, M. C. Hersam and S. Barlow, J. Am. Chem. Soc., 2020, 142, 783-791.
55 Y. Zhang, W. Zhang, Q. Li, C. Chen, Z. Zhang, *Sensors Actuators B Chem*., 2020, **324**, 128733
56 H. Singh, V. K. Tomer, N. Jena, I. Bala, N. Sharma, D. Nepak, A. D. Sarkar, K. Kailasam and S. K. Pal, *J. Mater. Chem. A*, 2017, **5**, 21820-21827.
57 S. Nandi, S. K. Singh, D. Mullangi, R. Illathvalappil, L. George, C. P. Vinod, S. Kurungot and R. Vaidhyanathan, Adv. Energy Mater., 2016, 6, 1601189.
58 D. Mullangi, V. Dhavale, S. Shalini, S. Nandi, S. Collins, T. Woo, S. Kurungot, R. Vaidhyanathan, Adv. Energy Mater., 2016, 6, 1600110.
59 S. Haldar, K. Roy, S. Nandi, D. Chakraborty, D. Puthusseri, Y. Gawli, S. Ogale and R. Vaidhyanathan, *Adv. Energy Mater.*, 2018, **8**, 1702170.
60 M. Frisch, G. Trucks, H. Schlegel, G. Scuseria, M. Robb, J. Cheeseman, G. Scalmani, V. Barone, B. Mennucci and G. Petersson, *Gaussian, Wallingford*, 2009.
61 N. Sun, Y. Jin, H. Wang, B. Yu, R. Wang, H. Wu, W. Zhou and J. Jiang, *Chem. Mater.*, 2022, 34, 1956–1964.
62 R. Maity, D. Chakraborty, S. Nandi, A. K. Yadav, D. Mullangi, C. Vinod and R. Vaidhyanathan, *ACS Appl. Nano Mater.*, 2019, **2**, 5169-5178.